ORIGINAL ARTICLE

A spatio-temporal deep learning model for enhanced atmospheric correction

Maitrik Shah[1] · Mehul S. Raval[1] · Srikrishnan Divakaran[2] · Debjyoti Dhar[3] · Hasit Parmar[4]

Abstract

Atmospheric correction (AC) is essential for accurate surface reflectance (SR) prediction, as it accounts for distortions in reflectance caused by atmospheric elements such as gases, aerosols, and water vapor. AC has diverse applications, including environmental monitoring, agricultural assessment, and climate studies. Traditional physics-based models for AC are often complex, require extensive calibration, and depend on atmospheric parameters, which can be challenging to obtain. In contrast, deep learning (DL) models offer simpler, more flexible, and extensible alternatives that exclusively rely on remote sensing satellite data. However, existing DL models for AC typically consider only spatial features, overlooking temporal variations in atmospheric conditions that are ucial for enhancing SR prediction accuracy. This paper introduces the Spatio-Temporal Atmospheric Correction (STAC) model, which integrates both spatial and temporal information to improve SR predictions. STAC outperforms the state-of-the-art Season-aware Atmospheric Correction Network (SAAC-Net), achieving a 30% reduction in root mean square error (RMSE) across multiple spectral bands. The model's generalisation ability is further demonstrated by evaluating diverse land cover types, where STAC achieved an average RMSE of 0.036, compared to 0.044 for SAAC-Net. Additionally, an assessment using the radiometric calibration network (RadCalNet) ground-measured dataset reveals that STAC achieves a mean relative difference (MRD) of 0.027, significantly outperforming both DL-based SAAC-Net (0.083) and physics-based land surface reflectance code (LaSRC) model (0.073). These results underscore the importance of incorporating temporal dynamics in DL-based AC models for enhanced atmospheric correction.

Keywords Atmospheric correction · Deep learning · Satellite images · Surface reflectance · Top of the atmosphere · Spatial-temporal features

✉ Maitrik Shah
  maitrikshah.ce@gmail.com

  Mehul S. Raval
  mehul.raval@ahduni.edu.in

  Srikrishnan Divakaran
  srikrishnan.divakaran@krea.edu.in

  Debjyoti Dhar
  deb@sac.isro.gov.in

  Hasit Parmar
  hasitparmar007@gmail.com

[1] School of Engineering and Applied Science, Ahmedabad University, Navrangpura, Ahmedabad, Gujarat 380015, India

[2] Department of Computer Science, Krea University, Appaiahpalem, Sricity, Andhra Pradesh, India

[3] Space Application Center, Indian Space Research Organization (ISRO), Ahmedabad, Gujarat 380015, India

[4] Computer Engineering Department, L D College of Engineering, Ahmedabad, Gujarat 380015, India

Introduction

Atmospheric correction (AC) is a critical process in remote sensing, essential for removing atmospheric distortions to ensure accurate surface reflectance (SR) measurements from satellite imagery. In recent years, the demand for medium to high-resolution and accurate remote sensing images of SR has surged, driven by their increasing use in land monitoring, emergency management, and security applications. To be truly effective, remote sensing images must be analysis-ready data (ARD), meaning they have undergone the necessary corrections for geometric distortions, radiometric calibration, atmospheric effects, and cloud masking, making them immediately usable without further preprocessing. Entities like Landsat and Sentinel provide ARD, and initiatives such as the Committee on Earth Observation Satellites (CEOS) (CEOS 2024) aim to standardize ARD

for consistent, easy use across applications (Potapov et al. 2020; Dwyer et al. 2018; Giuliani et al. 2018).

With the growing availability of Earth observation (EO) data and demand for ARD, accurate AC is a crucial pre-processing step in remote sensing (Doxani et al. 2023). The reflectance captured by satellites is called top-of-atmosphere (TOA) reflectance, which includes the effects of atmospheric scattering and absorption caused by various atmospheric elements (aerosols, water vapour, and gases). AC retrieves radiance values that accurately reflect the Earth's surface properties, known as SR or bottom-of-atmosphere (BOA) reflectance. SR is an essential parameter for numerous remote sensing applications, including biophysical parameters (Kganyago et al. 2021; Parida and Kumari 2021), crop type classification (Patel et al. 2023), water quality assessment (Brando and Dekker 2003; Ramaraj and Sivakumar 2023), climate studies (Saeidi et al. 2023; Angelopoulou et al. 2019) and land use and cover change (Verma and Raghubanshi 2019; Sabri et al. 2024) enabling accurate analysis and interpretation of satellite imagery across various domains.

Traditionally, AC relies on physics-based models like land surface reflectance code (LaSRC) (Vermote et al. 2016), which use radiative transfer calculations. These models are computationally intensive and time-consuming, leading to the use of Look-Up Tables (LUTs) for faster correction. However, constructing LUTs is complex and necessitates various atmospheric parameters—such as aerosol optical depth (AOD) and column water vapor (CWV)—to retrieve SR accurately. This process involves significant approximations that can introduce biases, particularly when estimating AOD and CWV. These limitations reduce the accuracy and generalisability of physics-based methods, especially in diverse environments. Moreover, Physics-based AC models rely on established relationships between atmospheric parameters and satellite observations. However, if these relationships change over time, such models do not extend and involve significant complexities in understanding atmospheric physics for building computationally accurate and efficient models (Kalnay 2003).

Deep learning (DL) has shown great potential in remote sensing tasks such as change detection, segmentation, and land use classification (Lin et al. 2020; Nijhawan et al. 2019; Saxena et al. 2020; Cheng et al. 2023). DL models, including convolutional neural networks (CNNs), autoencoders, and vision transformers, facilitate spectral, spatial, and temporal feature extraction (Gao et al. 2022; Chen et al. 2016; Romero et al. 2016; Tarasiou et al. 2023). These models can capture complex, non-linear relationships between TOA and BOA without relying on ancillary data or atmospheric parameters. For example, Duffy et al. (2022) developed a DL-based emulator for the MAIAC model, performing AC of hyperspectral images from the advanced Himawari imager (AHI) sensor on the Himawari-8 satellite. A more comprehensive approach to DL-based AC was given in Shah et al. (2023a). The authors proposed an end-to-end DL-based season-aware AC model named SAAC-Net with an extensive training dataset encompassing six different land covers (LC) of the Indian subcontinent. The model has shown promising results and generated BOA images that are similar to the reference BOA images.

While these DL models offer improved accuracy and computational efficiency over traditional physics-based models, they often overlook the temporal variability in atmospheric conditions. Over time, nearly every location on Earth experiences changes in atmospheric conditions. Atmospheric parameters such as AOD and CWV vary dynamically over time, creating a dataset shift problem for DL models (Shah et al. 2023b). This shift changes the relationships between TOA and SR, necessitating varying corrections for accurate SR prediction. Current DL models, including the state-of-the-art SAAC-Net, which utilises spatial and seasonal information, do not account for these temporal changes, leading to less accurate SR predictions as atmospheric conditions evolve.

To address this, we propose a novel DL model called Spatio-Temporal Atmospheric Correction (STAC), which integrates temporal information in addition to spatial and seasonal information to enhance prediction accuracy. To our knowledge, no prior research has explored AC using DL with spatio-temporal features. STAC incorporates two separate streams for spatial and temporal feature extraction, given in Fig. 2. "Model architecture and training" section provides a detailed description of model architecture. It leverages depthwise separable convolution (DSC), time-distributed convolution (TDC) and optical flow techniques to predict SR from TOA images. Optical flow computations on TOA images of five consecutive years in STAC capture temporal changes in atmospheric conditions, enabling the model to adapt and predict SR accurately.

The rest of the paper is organised as follows. "Materials and methods" section details the study area, the dataset, and the proposed approach. "Model architecture and training" section describes the model architecture, experimental setup and model training. "Result and discussions" section presents performance evaluation metrics and the model's performance assessment. Finally, "Conclusion" section summarises the findings and concludes the paper.

Materials and methods

This section describes the study area, the proposed approach, and the datasets used for training, testing, and validation. Additionally, it provides details on the Radiometric Calibration Network (RadCalNet) ground dataset used for performance benchmarking.

Study area

We chose urban land and cropland for training the STAC model because of their distinct surface properties and varying dynamic characteristics. Urban land typically exhibits higher reflectivity because of materials like concrete, asphalt, and metal, while cropland shows faster temporal variability due to changes in crop cycles. Additionally, both land types are heavily influenced by human activities: urban areas are affected by pollution and construction, whereas agricultural practices and crop growth shape croplands. These variations provide a robust dataset for training the model to handle diverse and evolving surface conditions.

Delhi (urban land; 28.7041°N, 77.1025°E) and Haryana (cropland; 29.0588°N, 76.0856°E) in India were the study areas used to train and test the model. Delhi, situated in northern India, experiences a diverse climatic and topographic landscape. It lies within a transition zone from the arid Thar desert in the west to the fertile Gangetic plains in the east. The mean annual temperature ranges from approximately 25–30 °C, with peak temperatures reaching 45 °C during summer. Precipitation levels vary significantly, with an average yearly rainfall of around 700 mm. Human activity and urbanization have transformed considerably its natural landscape, increasing pollution and environmental challenges. Delhi is considered one of the most polluted cities in the world (IQAir 2024). According to research, this region's AOD and CWV values have increased significantly over the years (Rai et al. 2020; Kumar et al. 2021; Patel and Kuttippurath 2022).

Haryana state is a region characterized by diverse climatic and topographic features. The mean annual temperature varies across the state, typically from 25 to 30 °C. Precipitation levels are relatively low, averaging between 400 and 600 mm annually, with variations depending on the specific location within the state. The majority of the LC of this region is cropland.

Proposed approach

The block diagram of the proposed approach, as shown in Fig. 1, outlines the two primary stages of the STAC model: pre-processing and model training. The TOA and BOA image pairs used in the study are acquired from the Landsat-8 Operational Land Imager (OLI) sensor (Roy et al. 2014). The OLI provides geometrically corrected and coregistered TOA and BOA image pairs at 30-m spatial and 16-day temporal resolutions. Each image has a size of 7681×7531 pixels with six spectral bands: Band 2 (0.45–0.51 µm)—Blue (B), Band 3 (0.53–0.59 µm)—Green (G), Band 4 (0.64–0.67 µm)—Red (R), Band 5 (0.85–0.88 µm)—Near-Infrared (NIR), Band 6 (1.57–1.65 µm)—Short-Wave Infrared 1 (SWIR1), and Band 7 (2.11–2.29 µm)—Short-Wave Infrared 2 (SWIR2). Band 1, the Coastal/Aerosol band (0.43–0.45 µm), was excluded from the analysis. In Landsat-8, the BOA images are generated from TOA images using the LaSRC physics-based AC algorithm (Vermote et al. 2016). The Landsat-8 data used for the study were obtained from the United States Geological Survey
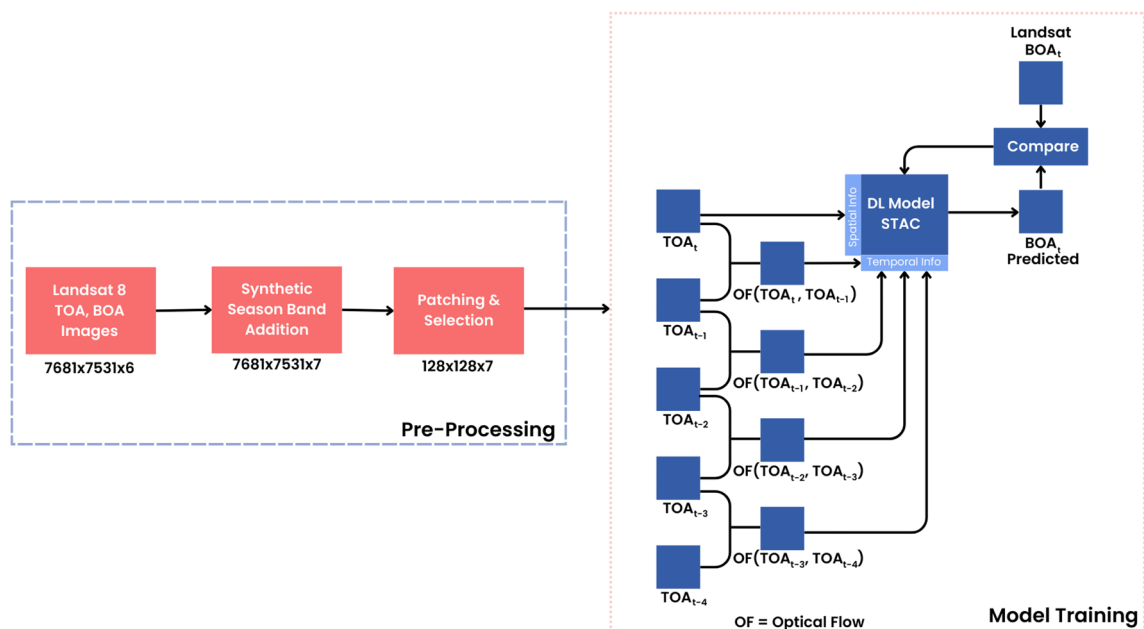

Fig. 1 Block diagram of the proposed approach

archives (https://earthexplorer.usgs.gov, last accessed on 14 September 2024).

A synthetic seasonal band was added as an additional input feature to help the model capture intra-annual seasonal variations. For this study, two distinct seasons in India-summer and winter-were considered, while the rainy season was excluded due to cloud cover complications. Only images with clear atmospheric conditions (less than 15% cloud cover) were used for the study. The synthetic season band is added as the seventh band in the images, with static values of 1 and 0 representing the summer and winter seasons, respectively. This inclusion is crucial because various atmospheric parameters, such as AOD and CWV, exhibit seasonal variations, affecting the reflectance values (Acharya and Sreekesh 2013; Randel et al. 2001). For instance, a previous study demonstrated that the mean TOA reflectance difference between summer and winter across different LC types is ≈ 0.04 (Shah et al. 2023a).

To enhance computational efficiency, the images were processed in patches. Each 7681×7531 image was divided into non-overlapping patches of 128×128 pixels, corresponding to an area of approximately 3.8 km$\times$ 3.8 km. This patch-based approach makes the data manageable for the DL model and ensures that the model effectively captures localised spatial information (Shah et al. 2023a). From each image, the 200 most informative patches, each sized 128×128 pixels, were selected based on entropy.

In training, the model inputs the target TOA image for the year t (TOA_t) along with optical flow images that capture temporal information. Four optical flow images are computed from TOA images over 5 years; target and past 4 years: $TOA_t, TOA_{t-1}, TOA_{t-2}, TOA_{t-3}, TOA_{t-4}$. This temporal data helps the model recognise how atmospheric parameters and reflectance change over time, which is critical for accurate SR prediction.

The TOA images and the optical flow outputs are fed into the deep DL model, STAC, designed to extract spatial and temporal features. The model processes these features to predict the BOA reflectance for the target year t. The predicted BOA is then compared with the reference or ground truth Landsat-8 BOA image to evaluate the model's accuracy. This comparison provides feedback for model optimization via backpropagation, allowing the model to improve continuously during training.

A comprehensive dataset was constructed meticulously to help the model learn intra-annual and inter-annual changes. Landsat-8 images of 2014 to 2022 of Delhi and Haryana were collected for the summer and winter seasons. For the summer season, most images are from April and May; for the Winter season, most are from November and December. Keeping images from nearby dates across multiple years allows the DL model to learn the change in the reflectance values. The details of the train and test datasets from the study area with acquisition dates are given in Table 1. The training dataset consists of images from 2018 to 2021, while images from 2022 are used to test the model's performance.

To check the model's generalisation capacity, its performance is also evaluated in regions other than where it is trained. The details of validation data are given in Table 2. Six LCs were used: urban land, cropland, deciduous forest, evergreen forest, fallow land, and wasteland. It is to be noted that the geographical locations representing urban land and cropland in the validation dataset given in Table 2 are different from the training set (Table 1).

Comparing SR predictions with actual ground measurements is necessary to validate the accuracy of STAC and ensure reliable data for analysis. It helps calibrate estimates with real-world conditions, ensuring their credibility. Therefore, data from the Radiometric Calibration Network (RadCalNet) (Bouvet et al. 2019) were utilised for analysis and benchmarking.

RadCalNet ground measurement dataset

RadCalNet, an initiative pioneered by the working group on calibration and validation under the CEOS, represents a pivotal advancement in satellite calibration and validation. This employs automated ground instruments to continuously monitor SR measurements and crucial atmospheric parameters across diverse RadCalNet sites. Operating at regular 30-min intervals from 09:00 to 15:00 local time, RadCalNet gathers data from 380 to 2500 nm with a spectral resolution of 10 nm. This comprehensive dataset facilitates the derivation of TOA, which is essential for refining and validating satellite-based observations, thus enhancing the accuracy and reliability of remote sensing applications.

The proposed work uses observations from the La Crau (43.55°N, 4.86°E) RadCalNet station in southeastern France as a reference to validate the model-predicted SR values. La Crau features a flat terrain with a dry Mediterranean climate. The predominant landscape consists of pebbles with sparse, low vegetation cover. To ensure consistency and comparability with the results presented in Doxani et al. (2023), we adopted the same observation period from October 2017 to September 2018. We found four scenes matching the RadCalNet measurement and the Landsat-8 capture dates (14.11.2017, 30.11.2017, 17.01.2018, 14.09.2018). Additionally, we collected scenes from the previous 4 years corresponding to these dates to provide auxiliary temporal data for the STAC model. The RadCalNet reflectance spectra are representative of a disk with a radius of 30 ms. Based on the spatial resolution of Landsat-8 and the representative region of RadCalNet, a 3×3 pixel resulting in a 90 m $\times$ 90 m region of interest is chosen for La Crau.

Table 1 Landsat-8 train and test datasets from the study area

Study area	Lat/Lon	Acquisition date of target images	Acquisition date of images of previous years
Delhi—Urban land 146040	28.7041°N, 77.1025° E	11.05.2018	16.05.2014, 03.05.2015, 21.05.2016, 24.05.2017
		05.12.2018	10.12.2014, 13.12.2015, 30.01.2016, 02.12.2017
		28.04.2019	03.05.2015, 21.05.2016, 24.05.2017, 11.05.2018
		08.12.2019	13.12.2015, 30.01.2016, 02.12.2017, 05.12.2018
		26.01.2020	30.01.2016, 02.12.2017, 05.12.2018, 08.12.2019
		16.05.2020	21.05.2016, 24.05.2017, 11.05.2018, 28.04.2019
		01.04.2021	24.05.2017, 11.05.2018, 28.04.2019, 16.05.2020
		29.12.2021	02.12.2017, 05.12.2018, 08.12.2019, 26.01.2020
		06.05.2022	11.05.2018, 28.04.2019, 16.05.2020, 01.04.2021
		16.12.2022	05.12.2018, 08.12.2019, 26.01.2020, 29.12.2021
Haryana—Crop land 147040	29.0588°N, 76.0856° E	10.01.2018	01.12.2014, 04.12.2015, 22.12.2016, 25.12.2017
		31.03.2018	07.05.2014, 26.05.2015, 12.05.2016, 15.05.2017
		29.01.2019	04.12.2015, 22.12.2016, 25.12.2017, 10.01.2018
		05.05.2019	26.05.2015, 12.05.2016, 15.05.2017, 31.03.2018
		07.05.2020	12.05.2016, 15.05.2017, 31.03.2018, 05.05.2019
		01.12.2020	22.12.2016, 25.12.2017, 10.01.2018, 29.01.2019
		26.05.2021	15.05.2017, 31.03.2018, 05.05.2019, 07.05.2020
		20.11.2021	25.12.2017, 10.01.2018, 29.01.2019, 01.12.2020
		13.05.2022	31.03.2018, 05.05.2019, 07.05.2020, 26.05.2021
		15.12.2022	10.01.2018, 29.01.2019, 01.12.2020, 20.11.2021

The study area shows the location, LC type and Landsat-8 rowpath. Images of years 2018–2021 are used for training, and images of years 2022 are used for testing

Model architecture and training

This section details the STAC model architecture, explaining how spatial and temporal features are extracted and integrated for SR prediction. It also describes the experimental setup and the model training process.

Model architecture

The proposed STAC model, as shown in Fig. 2, consists of three stages: (1) feature extraction, (2) feature fusion, and (3) prediction. In the feature extraction stage, the architecture is divided into two parallel pathways: The spatial and temporal channels. The spatial channel is responsible for extracting spatial features using depthwise separable convolution, while the temporal pathway focuses on extracting temporal features using optical flow computations and time-distributed convolution. These two pathways capture spatial variations and temporal dynamics, comprehensively representing the input data for accurate SR prediction.

The input to the spatial channel is the TOA image of the year t (TOA_t) for which we want to perform AC. The input image has dimensions of $128 \times 128 \times 7$, where 128×128 represents the spatial resolution of the image, and 7 refers to the number of channels: six spectral bands from Landsat-8

and one additional synthetic season band. Features are extracted from the input image using four DSC layers. DSC offers significant advantages over standard convolutions in DL architectures (Chollet 2017). By splitting the convolution process into depthwise and pointwise stages, these convolutions reduce the number of parameters and computations required, leading to more parameter-efficient and computationally efficient models (Kaiser et al. 2017). The depthwise stage applies filters independently to each input channel, capturing spatial information efficiently, while the pointwise stage combines these outputs across channels to create rich feature representations. This separation enhances the model's ability to learn diverse and expressive features while maintaining computational efficiency (Kaiser et al. 2017). LeakyReLU is an activation function used in the model that maintains a slight, non-zero slope for negative inputs, ensuring that neurons remain active and gradients flow consistently during training (Maas 2013). This characteristic promotes faster convergence, more stable training, and improved generalization of DL models. We used 3×3 convolution kernels throughout the model since deeper networks with small kernel sizes work well (Simonyan and Zisserman 2014).

The temporal pathway is designed to capture changes in atmospheric conditions over time using optical flow

Table 2 Validation dataset using Landsat-8 to check generalisation of the STAC

Study area	Lat/Lon	Acquisition dates of target images	Acquisition dates of images from previous years
Ahmedabad, Gujarat—Urban land 148044	23.0225° N, 72.5714° E	04.05.2022	09.05.2018, 12.05.2019, 14.05.2020, 15.04.2021
		30.12.2022	19.12.2018, 22.12.2019, 24.12.2020, 11.12.2021
Jalandhar, Punjab—Crop land 148039	31.3260° N, 75.5762° E	20.05.2022	25.05.2018, 29.05.2019, 12.04.2020, 17.05.2021
		14.12.2022	03.12.2018, 06.12.2019, 08.12.2020, 11.12.2021
Sukma, Chhattisgadh—Deciduous Forest 142045	18.3909° N, 81.6588° E	02.05.2022	15.05.2018, 18.05.2019, 04.05.2020, 07.05.2021
		20.12.2022	25.12.2018, 28.12.2019, 30.12.2020, 17.12.2021
Tamenglong, Manipur—Evergreen Forest 135043	24.9898° N, 93.5012° E	22.03.2022	28.04.2018, 30.03.2019, 01.04.2020, 19.03.2021
		03.12.2022	08.12.2018, 11.12.2019, 29.12.2020, 16.12.2021
Bikaner, Rajasthan—Fallow Land 149041	28.0229° N, 73.3119° E	19.05.2022	30.04.2018, 03.05.2019, 05.05.2020, 24.05.2021
		21.12.2022	26.12.2018, 29.12.2019, 15.12.2020, 18.12.2021
Jaisalmer, Rajasthan—Waste Land 150041	26.9157° N, 70.9083° E	18.05.2022	23.05.2018, 10.05.2019, 12.05.2020, 15.05.2021
		12.12.2022	17.12.2018, 04.12.2019, 06.12.2020, 09.12.2021

Study area list location, LC type and Landsat-8 rowpath
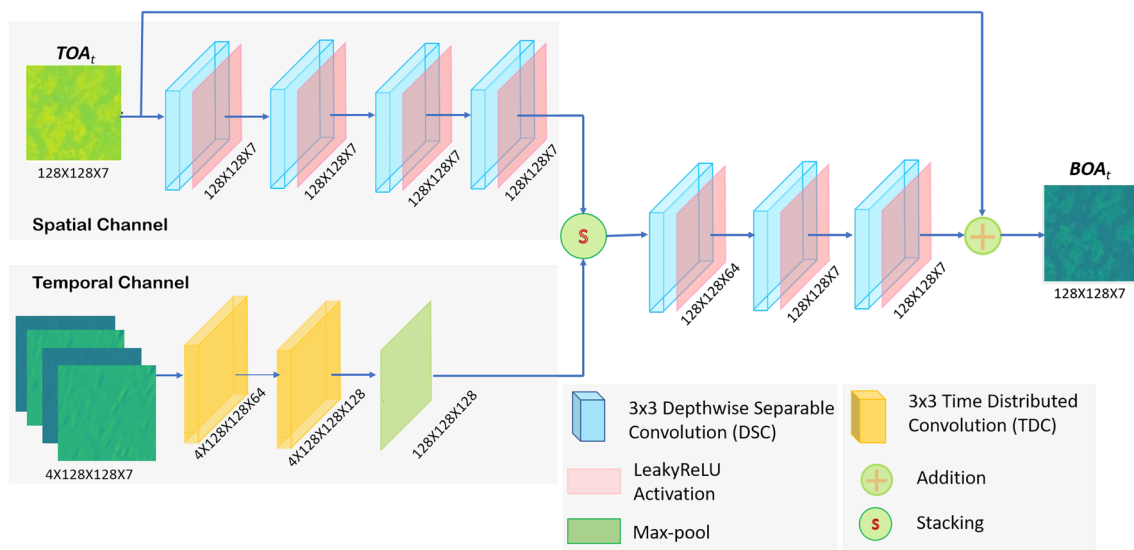
Fig. 2 Architecture of the proposed model—STAC having three stages. 1. Feature Extraction: Spatial and Temporal channels, 2. Feature Fusion: Stacking element S, 3. Prediction: Convolution and Relu units after stacking element S and addition operator

(Horn and Schunck 1981) and TDC. Optical flow is computed between consecutive TOA images over 5 years (TOA_t, TOA_{t-1}, TOA_{t-2}, TOA_{t-3}, TOA_{t-4}), capturing the motion

and temporal evolution of atmospheric parameters such as aerosol distribution and water vapour content. Optical flow computation estimates the motion of points between two

consecutive images, generating spatial and temporal gradients. By generating four optical flow images, we encapsulated the transformation and evolution of the atmosphere over 5 years, providing a dynamic view of temporal changes.

To process the optical flow images, TDCs (Mao et al. 2022) are applied. TDC applies convolutional layers independently to each optical flow image in the time series, preserving the temporal structure while extracting spatial features at each time step. TDC enables the model to manage temporal dependencies across consecutive years by sharing weights along the temporal dimension. This ensures that the same spatial features are extracted consistently from each time step, enabling the model to learn how atmospheric conditions change over time. To increase the model's capacity to learn complex temporal patterns, TDC is applied twice, progressively increasing the depth from 7 to 64 and then to 128. This gradual increase in depth allows the model to capture more detailed temporal features while balancing model complexity and overfitting. Experiments showed that further increasing the depth to 256 did not yield significant performance improvements, indicating that the chosen configuration (64 and 128 filters) provides optimal performance.

The output after the second TDC comprised four data cubes, each with dimensions 128 (height) × 128 (width) × 128 (depth). A max-pooling operation is then applied to these cubes, selecting the most relevant features and reducing noise, resulting in a single data cube. This operation also helps reduce computational complexity while preserving key spatial and temporal features.

In the feature fusion stage, the spatial and temporal features are combined. The spatial and temporal channels' outputs are stacked to create a unified feature representation. By fusing spatial and temporal information, the STAC model can simultaneously account for both spatial variations and temporal changes. Finally, in the prediction stage, the fused features undergo three convolutional layers with LeakyReLU activation to refine the feature set. An addition operator is then applied to combine the input TOA features with the final output, which serves as a residual connection, allowing the model to retain essential input information. The output of this stage is a BOA image of year t (BOA_t), representing the predicted SR.

Model training

The experimental configuration utilized a workstation with a 16GB GPU powered by an ×86-based Intel processor with NVIDIA Pascal architecture (P5000-6000). A patch size of 128 × 128 was chosen to balance spatial coverage and computational complexity. This decision was motivated by the understanding that increasing the patch size would result in a quadratic rise in the number of parameters, leading to higher memory demands. We maintained a learning rate of 0.001 throughout the training process, employed the L2 loss function, and utilized the ADAM optimizer with $\beta_1 = 0.9$ and $\beta_2 = 0.999$ values for improved convergence speed and stability. The entire code was implemented in Python, leveraging the Keras and TensorFlow open-source libraries.

The training process involved utilising urban and cropland regions of India (refer to Table 1). Images from 2018 to 2021 were utilized to facilitate model training. From each image, the 200 most informative patches, each sized at 128 × 128 pixels, were selected based on entropy, resulting in 3200 patches for training. Images of the year 2022 (refer to Table 1) were used for testing, and a total of 800 patches were used. Furthermore, to validate the model's generalisation ability, a comprehensive evaluation was conducted across six diverse LC types-urban areas, croplands, deciduous forests, evergreen forests, fallow lands, and wastelands-using two images for each type, totalling twelve images (refer to Table 2). From each image, 200 patches were selected, leading to 2400 image patches for validation. The results of this evaluation are discussed in the next section.

Result and discussions

This section outlines the metrics used to assess the model's performance and discusses the results obtained from the test, validation, and RadCalNet ground measurement data.

Evaluation metrics

In our study, we conducted statistical analyses and computed the root mean square error (RMSE) and correlation coefficient (CC) to evaluate the performance in estimating surface reflectance. These two are widely used statistical metrics for assessing the accuracy and consistency of model predictions against reference data. Lower RMSE (ideal 0) and higher CC (ideal 1) represent better predictions.

RMSE was used to quantify the statistical deviation between the SR values predicted by the model and those derived from Landsat-8 LaSRC. It is a reliable metric for assessing accuracy, offering straightforward interpretation and potential enhancements. The RMSE is calculated as below.

$$RMSE_\lambda = \sqrt{\frac{\sum_{i=1}^{n_\lambda}(\Delta\rho_{i,\lambda})^2}{n_\lambda}}. \tag{1}$$

$RMSE_\lambda$ is the RMSE value between the SR values predicted by the model and those derived from Landsat-8 LaSRC for band λ, n_λ is the number of pixels in band λ, $\Delta\rho_{i,\lambda}$ is the difference of model predicted SR values and Landsat-8 LaSRC SR values defined as below equation.

$$\Delta\rho_{i,\lambda} = \hat{\rho_{i,\lambda}} - \rho_{i,\lambda} \qquad (2)$$

where $\hat{\rho_{i,\lambda}}$ is the model predicted SR and $\rho_{i,\lambda}$ is the Landsat-8 LaSRC SR for pixel i in band λ.

A correlation coefficient was used to gauge the linear relationship between the SR values obtained from model predictions and those derived from reference images. This metric served as a measure of similarity, indicating the spatial consistency of our proposed model. By assessing the correlation coefficient, we gained valuable insights into the degree of agreement between the predicted reflectance values and the reference data, providing a comprehensive assessment of our approach's performance and spatial fidelity. The CC is calculated as below.

$$CC_{\lambda} = \frac{\sum_{i=1}^{n}(\rho_{i,\lambda} - \mu_{\rho,\lambda})(\hat{\rho_{i,\lambda}} - \hat{\mu_{\rho,\lambda}})}{\sqrt{\sum_{i=1}^{n}(\rho_{i,\lambda} - \mu_{\rho,\lambda})^2}\sqrt{\sum_{i=1}^{n}(\hat{\rho_{i,\lambda}} - \hat{\mu_{\rho,\lambda}})^2}}. \qquad (3)$$

CC_{λ} is the correlation coefficient between the Landsat-8 BOA image and the model-predicted BOA image for band λ. $\mu_{\rho,\lambda}$ and $\hat{\mu_{\rho,\lambda}}$ are the mean SR of Landsat-8 BOA image and model predicted image for band λ respectively.

Model assessment—test dataset

In this section, we evaluate the performance of the STAC model on the test dataset (ref. Table 1) by analysing RMSE and CC across all spectral bands. Furthermore, we conduct a comparative analysis with the state-of-the-art SAAC-Net model (Shah et al. 2023a) to demonstrate the effectiveness of the proposed STAC model in SR prediction.

Table 3 provides a comparative analysis of the performance of the proposed STAC model against the state-of-the-art SAAC-Net model. Particularly notable are the improvements in the green, red, NIR, and SWIR bands. The most substantial improvements in RMSE are observed in the red and NIR bands, both showing a 50% reduction, which is particularly relevant for applications like

Table 3 Band-wise performance of proposed STAC on test dataset (ref. Table 1) and comparison with SAAC-Net

Bands	STAC		SAAC-Net		% Improvement in RMSE
	RMSE	CC	RMSE	CC	
Blue	0.01	0.78	0.01	0.75	0
Green	0.009	0.91	0.016	0.7	43
Red	0.01	0.94	0.02	0.77	50
NIR	0.022	0.85	0.044	0.54	50
SWIR1	0.023	0.88	0.047	0.62	51
SWIR2	0.02	0.92	0.037	0.73	45
Average	0.017	0.88	0.024	0.68	30

vegetation monitoring, where these bands are critical for deriving indices such as the Normalized Difference Vegetation Index (NDVI). No improvement was observed in the blue band, where both models achieved an identical RMSE of 0.01. This suggests that while STAC is more effective in most spectral bands, both models face similar challenges in correcting atmospheric effects in the blue spectral region, where shorter wavelengths are more susceptible to scattering. Despite this, the STAC model demonstrates impressive performance, achieving an approximate 30% reduction in RMSE across all bands, with an average RMSE of 0.017 compared to SAAC-Net's 0.024.

The STAC model also consistently outperforms SAAC-Net regarding CC, with higher values across all spectral bands, demonstrating a stronger linear relationship between predicted and reference SR values. This indicates that the STAC model can better maintain spatial consistency and produce SR predictions that align more closely with reference data. Notably, in the SWIR2 band, the STAC model achieves a CC of 0.92, a marked improvement over SAAC-Net's CC of 0.73, further demonstrating the robustness of STAC in handling longer wavelength bands, which are often more sensitive to atmospheric variability.

Figure 3 compares the STAC and SAAC-Net models on a single 128×128 image patch of the urban LC (147040) using Landsat-8 data across different spectral bands. The predicted SR images generated by STAC exhibit closer visual alignment with the reference BOA images across all spectral bands than those generated by SAAC-Net. In particular, the STAC model better preserves fine spatial details and surface features, especially in the SWIR bands, where atmospheric distortions are typically more challenging to correct. The SAAC-Net model, by contrast, introduces more noise and exhibits less spatial fidelity, particularly in the NIR and SWIR bands, where its predictions are less consistent with the reference BOA images. This discrepancy can be attributed to SAAC-Net's reliance on a single TOA input, limiting its ability to adapt to temporal variations in atmospheric conditions. The RMSE values for the STAC-predicted images demonstrate better accuracy, with respective values of 0.012, 0.008, 0.006, 0.017, 0.016, and 0.013 for blue(B), green(G), red(R), NIR, SWIR1(S1), and SWIR2(S2) bands. In contrast, the RMSE values for SAAC-Net predictions are slightly higher: 0.008, 0.009, 0.011, 0.023, 0.026 and 0.020, respectively. The CC values further support this observation, as the STAC model achieves coefficients of 0.88(B), 0.96(G), 0.98(R), 0.94(NIR), 0.95(S1), and 0.97(S2) across the bands, indicating strong spatial consistency and agreement with Landsat-8 BOA images. Conversely, SAAC-Net exhibits lower coefficients, 0.88, 0.86, 0.90, 0.84, 0.88 and 0.92 across bands, suggesting less spatial agreement with the reference data.

Fig. 3 The first row shows Landsat-8 TOA images (**a–f**), the second row shows Landsat-8 BOA images (**g–l**), the third row shows STAC predicted images (**m–r**), Fourth row shows SAAC-Net predicted images (**s–x**) for urban land LC 147,040 for each band in order from left to right—Blue, Green, Red, NIR, SWIR1, SWIR2

(a) (b) (c) (d) (e) (f)
(g) (h) (i) (j) (k) (l)
(m) (n) (o) (p) (q) (r)
(s) (t) (u) (v) (w) (x)
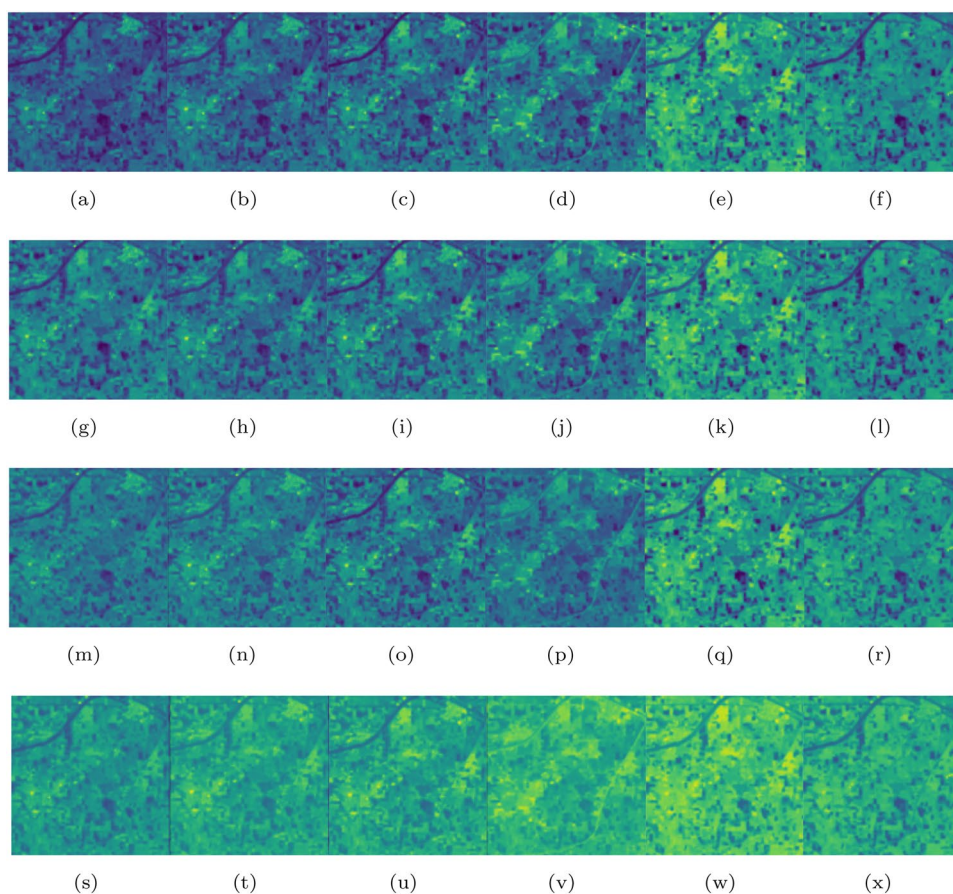
Model assessment—validation dataset

The generalisation ability of the STAC was assessed by evaluation of its performance across six LCs: urban land, cropland, deciduous forest, evergreen forest, fallow land, and wasteland (ref. Table 2), based on the International Geosphere-Biosphere Programme's global vegetation classification scheme (Loveland and Belward 1997). Given the diverse terrains and associated spectral signatures, these LC types offer a comprehensive test for the robustness of the model. The results of this experiment are given in Table 4.

The results presented in Table 4 indicate that the STAC model consistently outperforms SAAC-Net, achieving lower RMSE values across all LCs except for cropland, where both models perform equally. The most substantial improvements are seen in the wasteland, where STAC reduces RMSE by 38%, and fallow land, where the reduction reaches 26%. The wasteland and fallow land classes typically experience substantial atmospheric and environmental changes due to sparse vegetation and varying albedo, making them challenging for SR prediction models. STAC's ability to reduce errors in these classes highlights its robustness in handling dynamic surface conditions.

Table 4 Performance of proposed STAC on validation dataset (ref. Table 2) with six LCs and comparison with SAAC-Net. Note that the model is trained only on two LCs - urban and cropland

LC—Types	STAC		SAAC-Net		% Improvement in RMSE
	RMSE	CC	RMSE	CC	
Urban land—148044	0.027	0.99	0.034	0.96	20
Crop land—148039	0.032	0.95	0.032	0.94	0
Deciduous Forest—142045	0.073	0.96	0.088	0.99	17
Evergreen Forest—135043	0.035	0.99	0.039	0.98	10
Fallow land—149041	0.031	0.98	0.042	0.94	26
Waste land—150041	0.021	0.99	0.034	0.90	38
Average	0.036	0.98	0.044	0.95	20

The absence of improvement in RMSE was noted for the cropland LC, where both the STAC and SAAC-Net models produced identical values. This result may indicate that cropland, with its repetitive crop cycles and relatively stable atmospheric conditions during the study period, does not present as many challenges in terms of temporal variability,

thereby reducing the advantage of incorporating temporal features. Overall, the average RMSE of STAC model across all LCs is 0.036, compared to 0.044 for SAAC-Net, representing almost 20%

In addition to the improvements in RMSE, STAC also demonstrates higher CC across most LC types. In the urban land category, STAC achieves a CC of 0.99, compared to 0.96 for SAAC-Net, indicating a nearly perfect correlation between predicted and reference SR values. This level of accuracy is critical in urban environments, where complex surface materials and atmospheric pollutants can create significant challenges for accurate SR estimation. Similarly, STAC achieves a near-perfect CC of 0.99 for wasteland, compared to SAAC-Net's CC of 0.90.

Overall, the results from Table 4 demonstrate the generalization capability of the STAC model, as it shows substantial improvements in RMSE and CC across multiple LC types. The model's ability to adapt to diverse environmental conditions and maintain high levels of accuracy emphasizes the importance of integrating spatio-temporal features into deep learning-based AC models.

Model benchmarking—ground RadCalNet dataset

This section presents a comparison between the STAC, SAAC-Net, and Landsat-8 LaSRC AC models using the mean relative difference (MRD) and standard deviation of the relative differences, respectively, when compared to ground measurements from the RadCalNet site at La Crau, France. This experiment evaluates how well the predicted SR values from the models align with actual ground measurements, offering insights into each model's accuracy and consistency across various spectral bands. The predicted SR values generated by the model were averaged across designated areas per site and their spatial resolution. The mean relative difference (MRD) is calculated as below.

$$MRD = \frac{\rho^{Model} - \rho^{RadCalNet}}{\rho^{RadCalNet}}. \tag{4}$$

Here, ρ^{Model} is the average SR value obtained by the STAC/SAAC-Net/LaSRC model and the $\rho^{RadCalNet}$ is the average SR value obtained by the RadCalNet. Four scenes of LaCrau are used for this purpose.

Figure 4 illustrates the MRD between the predicted SR values from the three models (STAC, SAAC-Net and LaSRC) and the reference RadCalNet data across six spectral bands. The results demonstrate that the STAC model outperforms both SAAC-Net and LaSRC in most bands, achieving lower MRD values across the spectrum. The STAC model's MRD are 0.003(B), 0.012(G), 0.01(R), 0.01(NIR), 0.013(S1), and 0.1(S2) for the different bands respectively whereas for SAAC-Net they are 0.10(B), 0.07(G), 0.003(R),
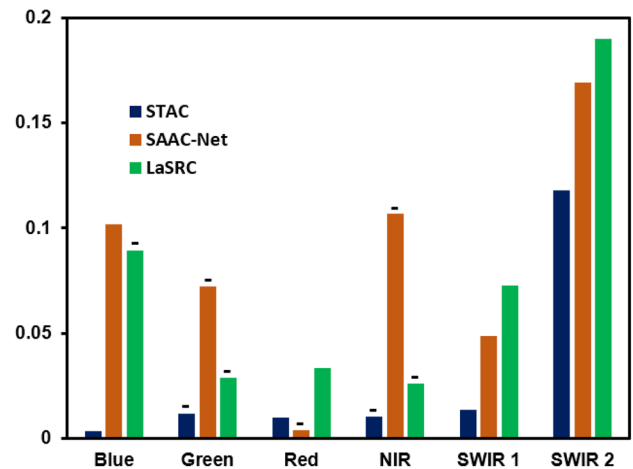

Fig. 4 Mean relative differences between the RadCalNet and model predicted SRs per band for LaCrau (France) site. X-axis: Landsat-8 spectral bands, Y-axis: Mean of relative difference. The minus sign (−) over the bars refers to underestimation in predictions by the model

0.10(NIR), 0.048(S1), 0.16(S2) and for LaSRC they are 0.08(B), 0.02(G), 0.03(R), 0.02(NIR), 0.07(S1) and 0.19 (S2). The STAC model's MRD is particularly low in the blue(B), green(G), and NIR bands, indicating minimal deviation from the reference data. In comparison, SAAC-Net shows significantly higher MRD values, especially in the blue(B) and NIR bands. At the same time, LaSRC exhibits moderate errors in most bands, with particularly high MRD in the SWIR2 band. Figure 4 shows that the STAC model overestimates SR, with exceptions observed in the green and NIR bands. The SAAC-Net underestimates SR in Green, Red and NIR bands. The LaSRC demonstrates underestimation in bands blue, green, and NIR while overestimating in other bands. The STAC model's overall mean MRD across all bands is 0.027, which represents a 67% reduction compared to SAAC-Net (0.083) and a 63% reduction compared to LaSRC (0.073). This substantial reduction in MRD underscores the effectiveness of the STAC model in producing SR predictions that are more closely aligned with RadCalNet ground measurements.

We also note that the MRD values of the STAC model are consistently lower than those of all other models tested in Doxani et al. (2023), except the SWIR2 band. The MRD values for STAC are significantly lower than the approximate MRD values obtained in Doxani et al. (2023) for ATCOR (Richter and Schläpfer 2019), a state-of-the-art physics-based atmospheric correction (AC) model. The corresponding MRD values for ATCOR are 0.02 (B), 0.06 (G), 0.08 (R), 0.07 (NIR), 0.04 (S1), and 0.05 (S2). This indicates the superior performance and accuracy of the STAC model in estimating SR across all spectral bands compared to traditional models like
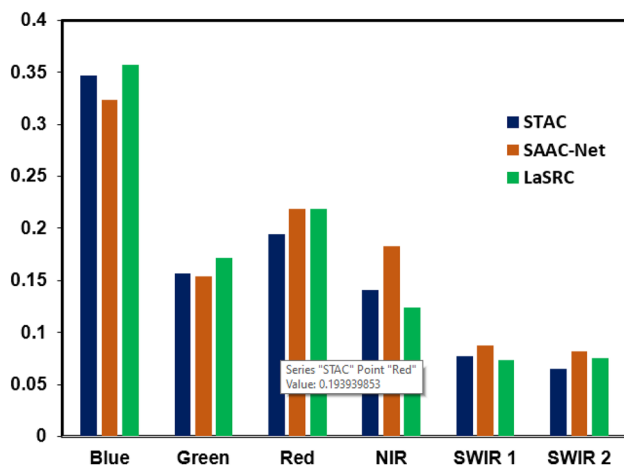
Fig. 5 Standard deviation of the relative differences between the Rad-CalNet and model predicted SRs per band for LaCrau (France) site. X-axis: Landsat-8 spectral bands, Y-axis: Standard deviation of the relative differences

ATCOR. This comprehensive validation process provides valuable insights into the performance of STAC relative to established state-of-the-art AC models, assessed in Doxani et al. (2023).

Figure 5 further evaluates the models by displaying the standard deviation of the relative differences between the predicted SR values and the RadCalNet measurements. The STAC model exhibits lower standard deviations across most bands, indicating more excellent stability and consistency in its predictions. Notably, the standard deviation for STAC in the blue band is relatively higher (0.3 to 0.4) than the other bands, suggesting that the blue spectral region remains challenging due to atmospheric scattering effects. However, even in the blue band, STAC outperforms both SAAC-Net and LaSRC, showing higher variability levels in their predictions. For the remaining bands, particularly in the short-wave infrared (SWIR) region, the STAC model significantly outperforms both SAAC-Net and LaSRC, with lower standard deviations indicating more consistent predictions. The STAC model demonstrates lower MRD than LaSRC, primarily due to its use of temporal data. In contrast, the physics-based LaSRC model does not incorporate temporal information and relies solely on instantaneous atmospheric conditions for correction. Additionally, LaSRC depends on atmospheric parameters such as AOD and CWV, which need to be estimated. Any inaccuracies in estimating these parameters can propagate errors in SR prediction, further highlighting the advantage of STAC's temporal feature integration.

Conclusion

In conclusion, this study presents the Spatio-Temporal Atmospheric Correction model, a novel deep learning framework designed to improve SR prediction in remote sensing by incorporating both spatial and temporal information. The model's integration of DSC, optical flow and TDC enables it to capture the complex atmospheric dynamics that occur over time, which traditional models fail to address. Incorporating auxiliary data from previous years enables STAC to adapt to temporal variations in atmospheric conditions, improving accuracy compared to the existing DL-model SAAC-Net. Across various spectral bands, STAC consistently outperforms SAAC-Net, achieving an average reduction in RMSE of 30%, with improvements of up to 50% in critical bands such as red and NIR, which are essential for vegetation monitoring and other applications. Furthermore, the model's performance on diverse LC types shows that STAC generalizes well, reducing RMSE by as much as 38% in challenging environments such as wastelands. The validation using the RadCalNet ground-measured dataset further reinforces the robustness and accuracy of STAC, where it exhibits a MRD that is 67% lower than SAAC-Net and 63% lower than LaSRC. These findings emphasise the importance of integrating spatiotemporal features into AC models for advancing remote sensing accuracy and reliability.

However, the proposed work has some limitations. First, the availability of historical data is limited, which may hinder the model's ability to capture long-term atmospheric variations comprehensively. Moreover, similar to many DL models, STAC faces challenges in interpretability, making it difficult to explain its internal decision-making process. Another limitation is the absence of uncertainty estimation in the predictions, which could affect the model's reliability in specific scenarios. Furthermore, the model is trained explicitly on Landsat-8 data, limiting its applicability for AC of images from other satellites. A potential solution would be implementing a transfer learning approach to adapt the model for other satellite platforms. Transformer-based architectures will be explored to improve the model's scalability and performance. Finally, future work will incorporate real-time processing capabilities to enable faster and more efficient SR predictions for practical applications.

Declarations

References

Acharya P, Sreekesh S (2013) Seasonal variability in aerosol optical depth over India: a spatio-temporal analysis using the MODIS aerosol product. Int J Remote Sens 34(13):4832–4849. https://doi.org/10.1080/01431161.2013.782114

Angelopoulou T, Tziolas N, Balafoutis A, Zalidis G, Bochtis D (2019) Remote sensing techniques for soil organic carbon estimation: a review. Remote Sens 11(6):676. https://doi.org/10.3390/rs11060676

Bouvet M, Thome KJ, Berthelot B, Bialek A, Czapla-Myers JS, Fox NP et al (2019) RadCalNet: a radiometric calibration network for earth observing imagers operating in the visible to shortwave infrared spectral range. Remote Sens 11:2401

Brando VE, Dekker AG (2003) Satellite hyperspectral remote sensing for estimating estuarine and coastal water quality. IEEE Trans Geosci Remote Sens 41(6):1378–1387. https://doi.org/10.1109/TGRS.2003.812907

CEOS (2024) CEOS analysis ready data. Accessed: 03 March 2024. https://ceos.org/ard/

Chen Y, Jiang H, Li C, Jia X, Ghamisi P (2016) Deep feature extraction and classification of hyperspectral images based on convolutional neural networks. IEEE Trans Geosci Remote Sens 54(10):6232–6251. https://doi.org/10.1109/TGRS.2016.2584107

Cheng X, Sun Y, Zhang W, Wang Y, Cao X, Wang Y (2023) Application of deep learning in multitemporal remote sensing image classification. Remote Sens 15(15):3859. https://doi.org/10.3390/rs15153859

Chollet F (2017) Xception: deep learning with depthwise separable convolutions. In: 2017 IEEE Conference on Computer Vision and Pattern Recognition (CVPR). IEEE Computer Society, Los Alamitos, CA, USA, pp 1800–1807. https://doi.ieeecomputersociety.org/10.1109/CVPR.2017.195

Doxani G, Vermote EF, Roger JC, Skakun S, Gascon F, Collison A et al (2023) Atmospheric Correction Inter-comparison eXercise, ACIX-II Land: an assessment of atmospheric correction processors for Landsat 8 and Sentinel-2 over land. Remote Sens Environ 285:113412. https://doi.org/10.1016/j.rse.2022.113412

Duffy K, Vandal TJ, Wang W, Nemani RR, Ganguly AR (2022) A framework for deep learning emulation of numerical models with a case study in satellite remote sensing. IEEE Trans Neural Netw Learn Syst. https://doi.org/10.1109/TNNLS.2022.3169958

Dwyer JL, Roy DP, Sauer B, Jenkerson CB, Zhang HK, Lymburner L (2018) Analysis ready data: enabling analysis of the landsat archive. Remote Sens 10(9):1363. https://doi.org/10.3390/rs10091363

Gao H, Chen Z, Xu F (2022) Adaptive spectral-spatial feature fusion network for hyperspectral image classification using limited training samples. Int J Appl Earth Observ Geoinf 107:102687. https://doi.org/10.1016/j.jag.2022.102687

Giuliani G, Chatenoux B, Honeck E, Richard JP (2018) Towards Sentinel-2 analysis ready data: a Swiss Data Cube Perspective. In: IGARSS 2018—2018 IEEE international geoscience and remote sensing symposium, pp 8659–8662

Horn BK, Schunck BG (1981) Determining optical flow. Artif Intell 17(1–3):185–203

IQAir (2024) World Air quality index. Accessed: 11 April 2024. https://www.iqair.com/in-en/world-air-quality-ranking

Kaiser L, Gomez AN, Chollet F (2017) Depthwise separable convolutions for neural machine translation. arXiv:abs/1706.03059

Kalnay E (2003) Atmospheric modeling, data assimilation and predictability. Cambridge University Press, Cambridge

Kganyago M, Mhangara P, Adjorlolo C (2021) Estimating crop biophysical parameters using machine learning algorithms and Sentinel-2 imagery. Remote Sens 13(21):4314. https://doi.org/10.3390/rs13214314

Kumar S, Singh A, Srivastava AK, Sahu SK, Hooda RK, Dumka UC et al (2021) Long-term change in aerosol characteristics over Indo-Gangetic Basin: How significant is the impact of emerging anthropogenic activities? Urban Clim 38:100880. https://doi.org/10.1016/j.uclim.2021.100880

Lin Y, Li S, Fang L, Ghamisi P (2020) Multispectral change detection with bilinear convolutional neural networks. IEEE Geosci Remote Sens Lett 17(10):1757–1761. https://doi.org/10.1109/LGRS.2019.2953754

Loveland TR, Belward AS (1997) The IGBP-DIS global 1km land cover data set, DISCover: first results. Int J Remote Sens 18(15):3289–3295. https://doi.org/10.1080/014311697217099

Maas AL (2013) Rectifier nonlinearities improve neural network acoustic models. https://api.semanticscholar.org/CorpusID:16489696

Mao K et al (2023) Prediction of depression severity based on the prosodic and semantic features with bidirectional LSTM and time distributed CNN. IEEE Trans Affective Comput 14(3):2251–2265. https://doi.org/10.1109/TAFFC.2022.3154332

Nijhawan R, Joshi D, Narang N, Mittal A, Mittal A (2019) A futuristic deep learning framework approach for land use-land cover classification using remote sensing imagery. In: Mandal JK, Bhattacharyya D, Auluck N (eds) Advanced computing and communication technologies. Springer Singapore, Singapore, pp 87–96

Parida BR, Kumari A (2021) Mapping and modeling mangrove biophysical and biochemical parameters using Sentinel-2A satellite data in Bhitarkanika National Park, Odisha. Model Earth Syst Environ 7:2463–2474. https://doi.org/10.1007/s40808-020-01005-3

Patel VK, Kuttippurath J (2022) Significant increase in water vapour over India and Indian Ocean: implications for tropospheric warming and regional climate forcing. Sci Total Environ 838:155885. https://doi.org/10.1016/j.scitotenv.2022.155885

Patel U, Pathan M, Kathiria P, Patel V (2023) Crop type classification with hyperspectral images using deep learning: a transfer learning approach. Model Earth Syst Environ 9:1977–1987. https://doi.org/10.1007/s40808-022-01608-y

Potapov P, Hansen MC, Kommareddy I, Kommareddy A, Turubanova S, Pickens A et al (2020) Landsat analysis ready data for global land cover and land cover change mapping. Remote Sens 12(3):426. https://doi.org/10.3390/rs12030426

Rai A, Singh RP, Shukla DP (2020) Source characterization of aerosols and trends during 2000–2019 Over Delhi (India). In: IGARSS 2020—2020 IEEE International Geoscience and Remote Sensing Symposium, pp 5517–5520

Ramaraj M, Sivakumar R (2023) Integration of band regression empirical water quality (BREWQ) model with deep learning algorithm in spatiotemporal modeling and prediction of surface water quality parameters. Model Earth Syst Environ 9:3279–3304. https://doi.org/10.1007/s40808-023-01695-5

Randel WJ, Wu F, Gettelman A, Russell JM III, Zawodny JM, Oltmans SJ (2001) Seasonal variation of water vapor in the lower stratosphere observed in Halogen Occultation Experiment data. J Geophys Res Atmos 106(D13):14313–14325. https://doi.org/10.1029/2001JD900048

Richter R, Schläpfer D. (2019) Atmospheric and topographic correction (ATCOR theoretical background document). DLR IB

Romero A, Gatta C, Camps-Valls G (2016) Unsupervised deep feature extraction for remote sensing image classification. IEEE Trans Geosci Remote Sens 54(3):1349–1362. https://doi.org/10.1109/TGRS.2015.2478379

Roy DP, Wulder MA, Loveland TR, Woodcock CE, Allen RG, Anderson MC et al (2014) Landsat-8: science and product vision for terrestrial global change research. Remote Sens Environ 145:154–172. https://doi.org/10.1016/j.rse.2014.02.001

Sabri A, Bahi H, Bounoua L, Tahiri M, Tweed S, LeBlanc M et al (2024) Predictive modelling on Spatial-temporal Land Use and Land Cover changes at the Casablanca-Settat Region in Morocco. Model Earth Syst Environ. https://doi.org/10.1007/s40808-024-02107-y

Saeidi V, Seydi ST, Kalantar B, Ueda N, Tajfirooz B, Shabani F (2023) Water depth estimation from Sentinel-2 imagery using advanced machine learning methods and explainable artificial intelligence. Geomat Nat Hazards Risk 14(1):2225691. https://doi.org/10.1080/19475705.2023.2225691

Saxena N, Raman B. (2020) Semantic segmentation of multispectral images Using Res-Seg-net model. In: 2020 IEEE 14th international conference on semantic computing (ICSC), pp 154–157

Shah M, Raval MS, Divakaran S, Dhar D, Parmar H (2023a) SAAC-Net: deep neural network-based model for atmospheric correction in remote sensing. Int J Remote Sens 44(23):7365–7389. https://doi.org/10.1080/01431161.2023.2282407

Shah M, Raval MS, Divakaran S, Patel P (2023b) Study and impact analysis of data shift in deep learning based atmospheric correction. In: IGARSS 2023—2023 IEEE International Geoscience and Remote Sensing Symposium, pp 6728–6731

Simonyan K, Zisserman A (2014) Very deep convolutional networks for large-scale image recognition. CoRR arXiv:abs/1409.1556

Tarasiou M, Chavez E, Zafeiriou S (2023) ViTs for SITS: vision transformers for satellite image time series. arXiv:2301.04944 [cs.CV]

Verma P, Raghubanshi AS (2019) Rural development and land use land cover change in a rapidly developing agrarian South Asian landscape. Remote Sens Appl Soc Environ 14:138–147. https://doi.org/10.1016/j.rsase.2019.03.002

Vermote E, Justice C, Claverie M, Franch B (2016) Preliminary analysis of the performance of the Landsat 8/OLI land surface reflectance product. Remote Sens Environ 185:46–56. https://doi.org/10.1016/j.rse.2016.04.008